Search for diboson resonances with CMS and Pixel Barrel Detector Calibration and Upgrade

Dissertation

zur
Erlangung der naturwissenschaftlichen Doktorwürde
(Dr. sc. nat.)

vorgelegt der Mathematisch-naturwissenschaftlichen Fakultät
der
Universität Zürich

von
Jennifer Ngadiuba

Promotionskomitee

Prof. Dr. Benjamin Kilminster
Prof. Dr. Florencia Canelli
Prof. Dr. Laura Baudis
Prof. Dr. Ueli Straumann

Zürich 2016

Contents

1 Introduction **1**

2 The Standard Model and beyond **2**
2.1 The Standard Model . . . 2
2.1.1 Particles and interactions . . . 2
2.1.2 Spontaneous symmetry breaking . . . 2
2.1.3 The Higgs mechanism . . . 2
2.1.4 The Higgs boson discovery at LHC . . . 2
2.2 The hierarchy problem and other SM limitations . . . 2
2.3 Theories of new physics . . . 2
2.3.1 Warped Extra dimensions . . . 2
2.3.2 Compositeness . . . 2
2.3.3 Heavy vector triplet . . . 2

3 The CMS Experiment at the LHC **3**
3.1 The Large Hadron Collider . . . 3
3.2 The CMS Detector . . . 6
3.2.1 Tracking detectors . . . 8
3.2.2 The Electromagnetic Calorimeter . . . 8
3.2.3 The Hadronic Calorimeter . . . 8
3.2.4 The Muon System . . . 8
3.2.5 The Trigger System . . . 8
3.3 The CMS detector simulation . . . 8

I Search for diboson resonances with CMS **10**

4 Diboson resonances as signature for new physics **11**

5 Event simulation **12**
5.1 Monte Carlo event generators . . . 12
5.2 Simulation of physics processes . . . 12
5.2.1 Simulation of signal processes . . . 12
5.2.2 Simulation of background processes . . . 12

6 Object and event reconstruction **13**
6.1 Tracks and vertices . . . 13
6.2 Electrons . . . 13
6.3 Muons . . . 13
6.4 Jets . . . 13
6.4.1 Identification of b jets . . . 13
6.5 Missing transverse energy . . . 13
6.6 W$\to \ell\nu$ reconstruction . . . 13

7 Boosted H→b$\bar{\text{b}}$ and W/Z→q$\bar{\text{q}}^{(\prime)}$ identification with jet substructure 14
7.1 Jet substructure algorithms . . . 14
7.1.1 Jet pruning . . . 14
7.1.2 N-subjettiness . . . 14
7.2 W/Z-tagging validation in top enriched sample . . . 14
7.3 H-tagging algorithm . . . 14

8 Final event selection and categorization 15
8.1 Search for a WH resonance in the $\ell\nu$b$\bar{\text{b}}$ final state at $\sqrt{s} = 8$ TeV . . . 15
8.1.1 $t\bar{t}$ background rejection . . . 15
8.1.2 Final selection and control plots . . . 15
8.2 Search for WW/WZ resonances in the $\ell\nu$q$\bar{\text{q}}^{(\prime)}$ final state at $\sqrt{s} = 13$ TeV . . . 15
8.2.1 W/Z-jet mass categories . . . 15
8.2.2 Final selection and control plots . . . 15

9 Background modeling 16
9.1 W+jets background estimate with alpha method . . . 16
9.1.1 Description . . . 16
9.1.2 Extraction of the W+jets normalization . . . 16
9.1.3 Extraction of the W+jets shape . . . 16
9.2 Top quark production . . . 16
9.3 Systematic uncertainties in the background estimation . . . 16

10 Signal modeling and statistical treatment 17
10.1 Signal modeling . . . 17
10.1.1 Parametrization of the resonance mass . . . 17
10.1.2 Signal efficiency . . . 17
10.2 Systematic uncertainties in the signal prediction . . . 17
10.3 Testing new resonance hypothesis . . . 17
10.3.1 Profile likelihood procedure . . . 17
10.3.2 The CL_s method . . . 17
10.3.3 Treatment of uncertainties . . . 17

11 Results with 8 TeV data 18
11.1 Final m_{WH} distribution . . . 18
11.2 Studies on the excess . . . 18
11.3 Significance of the data . . . 18
11.4 Cross section limits . . . 18

12 Results with 13 TeV data 19
12.1 Final m_{WV} distribution . . . 19
12.2 Cross section limits . . . 19

13 Combination of searches for diboson resonances at $\sqrt{s} = 8$ and 13 TeV 20
13.1 Inputs to the combination . . . 20
13.1.1 8 TeV VV searches . . . 20
13.1.2 13 TeV VV searches . . . 20
13.1.3 8 TeV VH searches . . . 20
13.1.4 13 TeV VH searches . . . 20
13.2 Combination procedure . . . 20

13.3 Results . . . 20
13.3.1 Limits on W' . . . 20
13.3.2 Limits on Z' . . . 20
13.3.3 Limits on heavy vector triplet (W'+Z') . . . 20
13.3.4 Limits on Bulk Graviton . . . 20
13.3.5 Significance at 2 TeV . . . 20

14 Conclusions **21**

II Calibration and Upgrade of the CMS Pixel Barrel Detector **22**

15 introduction chapter: why pixels are so important for physics **23**

16 The CMS Pixel Barrel Detector **24**
16.1 Design of the CMS Pixel Barrel Detector . . . 24
16.2 Detector modules . . . 24
16.2.1 Sensor . . . 24
16.2.2 Readout Chip . . . 24
16.2.3 Token Bit Manager . . . 24
16.3 Readout and control system . . . 24
16.3.1 Analog readout chain . . . 24
16.3.2 Front End Driver . . . 24
16.3.3 Supply Tube . . . 24
16.3.4 Communication and Control Unit . . . 24
16.3.5 Front End Controller . . . 24
16.4 Pixel Online Software . . . 24
16.5 Performance at $\sqrt{s} = 8$ and 13 TeV . . . 24

17 Optimization and commissioning for LHC Run II **25**
17.1 Radiation damage after LHC Run I . . . 25
17.2 Optimization for LHC Run II . . . 25
17.2.1 Overview of pixel calibrations . . . 25
17.2.2 Temperature dependence . . . 25
17.3 Commissioning for LHC Run II . . . 25
17.3.1 Installation into CMS . . . 25
17.3.2 Check out of optical connections . . . 25
17.3.3 Adjustment of readout chain settings . . . 25
17.3.4 Optimisation of signal performance . . . 25

18 Phase I Upgrade of the CMS Pixel Barrel Detector **26**
18.1 Motivations . . . 26
18.2 Summary of changes . . . 26
18.3 The digital readout chain . . . 26
18.4 The Phase I supply tubes . . . 26
18.5 The test stand . . . 26
18.6 Supply tubes assembly and commissioning . . . 26
18.7 Detector commissioning . . . 26

19 Conclusions **27**

III Summary **28**

Bibliography **30**

Chapter 1

Introduction

Chapter 2

The Standard Model and beyond

2.1 The Standard Model

2.1.1 Particles and interactions

2.1.2 Spontaneous symmetry breaking

2.1.3 The Higgs mechanism

2.1.4 The Higgs boson discovery at LHC

2.2 The hierarchy problem and other SM limitations

2.3 Theories of new physics

2.3.1 Warped Extra dimensions

2.3.2 Compositeness

2.3.3 Heavy vector triplet

Chapter 3

The CMS Experiment at the LHC

3.1 The Large Hadron Collider

The Large Hadron Collider (LHC) [1] is a proton-proton (pp) collider located at the European Particle Physics Laboratory (CERN) near Geneva, Switzerland. It is situated in the former CERN Large Electron-Positron Collider (LEP) tunnel with a circumference of 27 km about 100 m under ground crossing the border between France and Switzerland. A hadron collider has been chosen to allow higher center-of-mass energies ($\sqrt{s}$) compared to electron-positron colliders, the latter limited by synchrotron radiation due to the low mass of the particles to be accelerated. High centre of mass energies are required for the production of heavy SM particles such as the top quark and the Higgs boson, and to search for new BSM interactions at the TeV scale. For this purpose, the LHC is designed to produce pp collisions up to a center-of-mass energy of 14 TeV, superseding previous high energy hadron colliders by a factor of 7. In addition to colliding protons, the LHC is also capable of accelerating and colliding heavy nuclei, which is, however, not considered in this work.

The LHC is the final element in a succession of machines that accelerate protons to increasingly higher energies. Protons, obtained from a hydrogen source, are first accelerated by a linear accelerator (LINAC 2) to energies of 50 MeV. The beam is then injected into the Proton Synchrotron Booster (PSB), which accelerates the protons to 1.4 GeV, followed by the Proton Synchrotron (PS), which pushes the beam to 25 GeV. Protons are then sent to the Super Proton Synchrotron (SPS) where they are accelerated to 450 GeV. Finally, the beam is injected in the LHC ring, where it completes several revolutions to reach the targeted energy. The LHC ring and the acceleration chain are sketched in Fig. 3.1.

Inside the ring, the two proton beams circulate in opposite directions in two tubes kept at ultrahigh vacuum, referred as beam pipes. The acceleration of protons inside LHC is made by radio-frequency cavities (400 MHz), giving a 492 keV energy gain per revolution, with a 7 keV loss per turn due to synchrotron radiation. It takes 4 minutes and 20 seconds to fill each LHC ring, and 20 minutes for the protons to reach their maximum energy of 7 TeV. The maximum energy of the protons is limited by the strength of the magnetic field required for keeping the protons inside the ring. For 7 TeV-protons a magnetic field of 8.3 T has to be produced, which can only be reasonably obtained by superconducting magnets. The ring is equipped with 1232 dipole magnets for bending and 392 quadrupole magnets for focussing made of niobium-titanium (NbTi), which are cooled down to a temperature of 1.9 K with the help of super-fluid helium. After acceleration the protons move through the ring in separate bunches of protons with a fixed spatial separation.

The LHC ring has four interaction points at which the two counter rotating beams are made to cross and located in the center of the four LHC experiments. Just prior to collision, particles from the incoming beams must be squeezed closer together in order to maximize the chances of interaction. For this purpose, a system of three quadrupole magnets, so-called inner triplet, is located at both sides of each interaction point, which squeeze the beams and lead them to collisions in the center of the detector. Inner triplets tighten the beam, making it 12.5 times narrower from 0.2 mm down to 16 μm across.

Besides the high center-of-mass energy required for the production of heavy particles, a high event rate has to be obtained to allow the discovery of processes with low production cross sections. The instantaneous luminosity $\mathcal{L}$ characterizes the interaction rate. For a process with a cross section σ, the interaction rate is given by

$$\frac{dN_{ev}}{dt} = \sigma\mathcal{L}. \tag{3.1}$$

The instantaneous luminosity depends only on the beam parameters and can be written for a Gaussian beam distribution as:

$$\mathcal{L} = \frac{N_b^2 n_b f_{\text{rev}} \gamma_r}{4\pi\sigma_x\sigma_y} \ , \tag{3.2}$$

where N_b is the number of particles per bunch, n_b the number of bunches per beam, f_{rev} the revolution frequency, γ_r the relativistic gamma factor, while σ_x and σ_y characterize the widths of the transverse beam profiles in the horizontal and vertical direction, respectively. The number of interaction events in a period of running time of the collider can be derived as

$$N_{ev} = \sigma \int \mathcal{L}dt = \sigma L \ , \tag{3.3}$$

where L is called the integrated luminosity. It is a measurement of the collected data size and it is usually expressed in inverse of cross section.

The LHC beams can reach very high luminosity with a high frequency bunch crossing and a high density of protons per bunch. In the ring, 2808 bunches of $1.15{\cdot}10^{11}$ protons are circulated, with an average length of 7.5 cm, a width of about 16 μm and a bunch spacing of 25 ns (collision frequency of 40 MHz). This corresponds to the design instantaneous luminosity of $10^{34}\,\text{cm}^{-2}\,\text{s}^{-1}$ for pp collisions, which supersedes by a factor of 100 the luminosity reached by previous hadron colliders.

Proton collisions take place in four points of the LHC tunnel where the four main experiments are located: ATLAS (*A Toroidal LHC ApparatuS*) [2], CMS (*Compact Muon Solenoid*) [3], LHCb (*LHC beauty experiment*) [4] and ALICE (*A Lead Ion Collider Experiment*) [5]. ATLAS and CMS are general purpose experiments, designed to get an extensive study of SM and BSM physics and to operate at the design luminosity. The LHCb experiment is instead optimized for bottom quark physics studies while the ALICE experiment is dedicated to the study of the lead-lead collisions at the design luminosity of $10^{27}\,\text{cm}^{-2}\,\text{s}^{-1}$.

LHC operation officially started at the beginning of September 2008 but it was interrupted after a short period, due to the breakdown of superconducting magnets. The collider has been reactivated in November 2009 with first pp collisions at $\sqrt{s} = 900$ GeV, officially starting a new era in the particle physics experiments. The operating center-of-mass energies in pp collisions have so far been 7 TeV in 2010-2011, 8 TeV in 2012 and 13 TeV in 2015-2016. The 7 and 8 TeV periods together make out the *LHC Run 1*, while the 13 TeV period is called the *LHC Run 2*. The work presented in this document is based on both dataset collected at 8 TeV in 2012 and at 13 TeV in 2015.

In the whole Run 1, the LHC operated with a 50 ns bunch spacing. The peak of instantaneous luminosity in 2011 has been $\sim 0.4{\cdot}10^{34}\,\text{cm}^{-2}\,\text{s}^{-1}$ with a total delivered integrated luminosity of 6.1 fb^{-1} [7]. In 2012 the beam energy increased to 4 TeV per beam with a peak luminosity of $\sim 0.8{\cdot}10^{34}\,\text{cm}^{-2}\,\text{s}^{-1}$ and 23.3 fb^{-1} delivered integrated luminosity by the end of that year [7]. The increment of the instantaneous luminosity leads to a no more negligible number of simultaneous interactions per bunch crossing, the so-called *pileup* (PU) events.

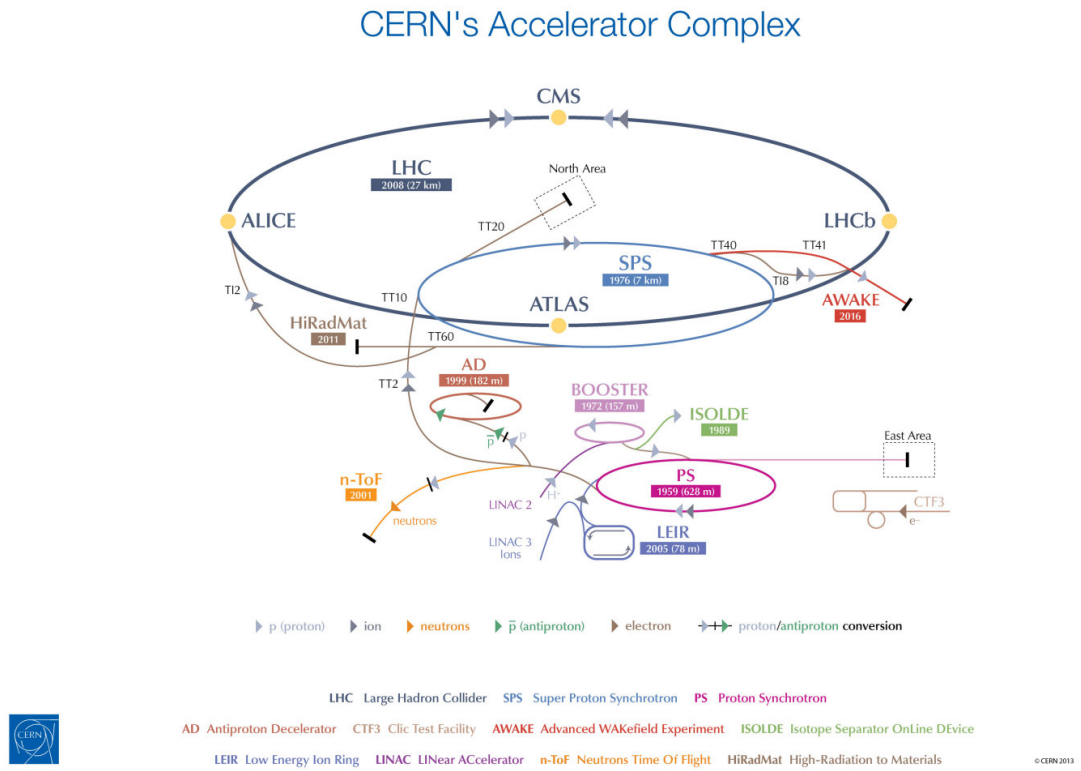

Figure 3.1: The LHC scheme together with its injection chain and the locations of the four main experiments ATLAS, CMS, LHCb and ALICE [6].

It depends on the cross section of inelastic collisions (75 mb at $\sqrt{s} = 8$ TeV [8]) and it is directly linked to the instantaneous luminosity. The average PU of the data collected in 2012 is equal to 21 (Fig. 3.2) while it has been around 15 in 2011 [7].

A shut-down period for the LHC (LS1) occurred in the whole 2013 and 2014, where upgrades and technical improvements have been performed in order to reach the designed instantaneous luminosity and center-of-mass energy. On March, 21st 2015 the first pp collisions at $\sqrt{s} = 13$ TeV has been obtained, a new record-breaking energy. For the first three months the machine operated with 50 ns bunch spacing while, from August 2015, it has been reduced to the designed 25 ns and the number of bunches per beam has been increased. The first part of this Run 2 phase ended on November 2015 with a total delivered integrated luminosity of 4.2 fb^{-1} and a peak luminosity of $\sim 0.5{\cdot}10^{34}\,\text{cm}^{-2}\,\text{s}^{-1}$ with an average pileup of 12 [7].

The LHC Run 2 has been restarted in April 2016, after an end-of-the-year technical stop, reaching a peak luminosity of $\sim 1.2{\cdot}10^{34}\,\text{cm}^{-2}\,\text{s}^{-1}$ (change this number at some point). The machine has remained in operation at $\sqrt{s} = 13$ TeV for the whole year with a total delivered integrated luminosity of 30 fb^{-1} (change this number at some point). Accordingly to the current LHC schedule, the Run 2 will proceed up to the end of 2018 with a total expected integrated luminosity of 100 fb^{-1}. The data collected in 2016 are not considered in this work.

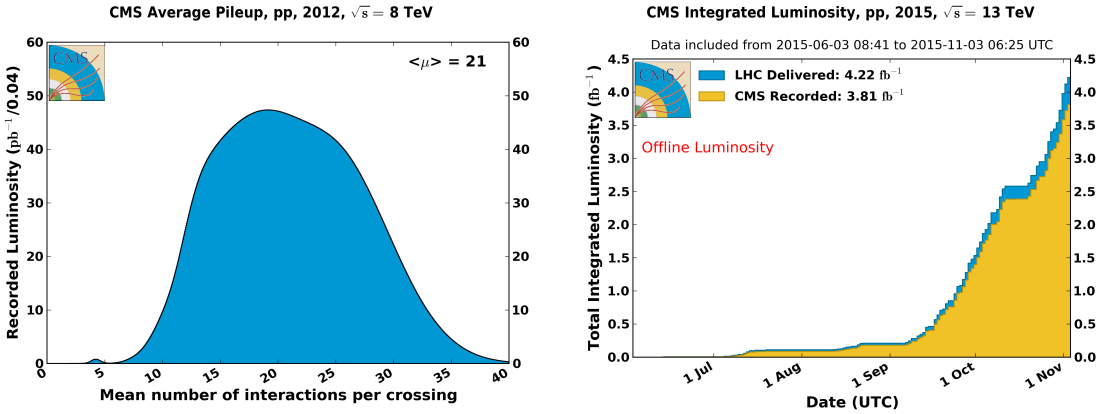

Figure 3.2: Mean number of interactions per bunch crossing in data collected in 2012 by the CMS experiment at LHC (left). Cumulative luminosity versus day (right) delivered by LHC (blue) in 2015; the off-line luminosity recorded by the CMS experiment is also reported (orange). [7]

3.2 The CMS Detector

The CMS detector is a general purpose detector installed 100 m underground at the LHC interaction point 5 (P5) near the village of Cessy in France. It has been designed to exploit the different properties of the wide range of particles and phenomena produced in high-energy collisions in the LHC. The design of the CMS detector is driven by the challenges of a physics experiment in the LHC environment. Many of the physics benchmark channels have a small cross section and the background from QCD jet production is overwhelmingly dominant. In order to achieve high rejection power with an optimal efficiency for rare channels, the detector has to be able to reconstruct the primary interaction entirely and to reduce the influence of overlapping events. Therefore, one needs to collect all possible information on the particles passing through the detector. Since these have different properties, a mixture of sub-detectors is required for a complete event reconstruction. The reconstruction of lepton signatures is essential for the extraction of rare processes and an excellent muon and electron identification and momentum resolution is desired. A precise measurement of secondary vertices and impact parameters is necessary for an efficient identification of heavy flavor quarks and τ-leptons. Moreover, a large hermetic geometric coverage is preferred, which allows for a precise estimate of the transverse momentum carried away by invisible particles through the sum of all visible particles.

The high peak luminosities of LHC lead to large pileup imposing further challenges to the design. As a consequence of pileup, the products of an interaction under study may be confused with those from other interactions in the same bunch crossing. This effect can be reduced by using high-granularity detectors resulting in low occupancy. In addition, the short bunch crossing requires fast response time and good time resolution of each detector element in order to discriminate the interaction under study from the interactions occurring in neighboring bunch crossings. Hence, a large number of detector channels and an excellent synchronization among them are required. Another challenge arises from the large flux of particles near the interaction point which leads to high radiation levels and the need of radiation hard detectors and front-end electronics.

Figure 3.3 shows the layout of the CMS detector. The detector is built in a cylindrical structure composed of a barrel in the center and endcaps at both sides. This structure is

21.6-m-long, 14.6-m in circumference and 12500-tons- heavy. The detector design and layout was driven by the choice of the magnetic field configuration. Large bending power is needed for a precise measurement of the momentum of high-energy charged particles. Within the CMS detector this is achieved by a superconducting solenoid with a length of 12.9 m and an inner diameter of 5.9 m generating a magnetic field of 4 T. The bore of the magnet coil is large enough to accommodate the inner tracker and the calorimetry inside. The inner tracker consists of a pixel and a strip detector both made out of Silicon, and it is the key component of CMS to measure the momenta of charged particles and identify primary and secondary vertices. The calorimetry system comprises a crystal electromagnetic calorimeter (ECAL) and a brass and scintillator hadronic calorimeter (HCAL), which provide information on the energies and directions of all charged and neutral particles. Outside the magnet are the large muon detectors, which, integrated inside the return yokes of the magnet, provide identification of muons and measurement of their momenta.

For the description of the CMS detector the following coordinate system is used. The origin is centered at the nominal collision point inside the experiment with the y-axis pointing vertically upward, the x-axis pointing radially inward toward the center of the LHC, and the z-axis points along the beam direction. The azimuthal angle ϕ is measured from the x-axis in the x-y plane. The polar angle θ is measured from the z-axis. Pseudorapidity is defined as η = -ln tan(θ/2). Thus, the momentum and energy measured transverse to the beam direction, denoted by p_{T} and E_{T}, respectively, are computed from the x and y components.

In the following sections the three main components of the CMS detector will be described together with a section on the triggering system.

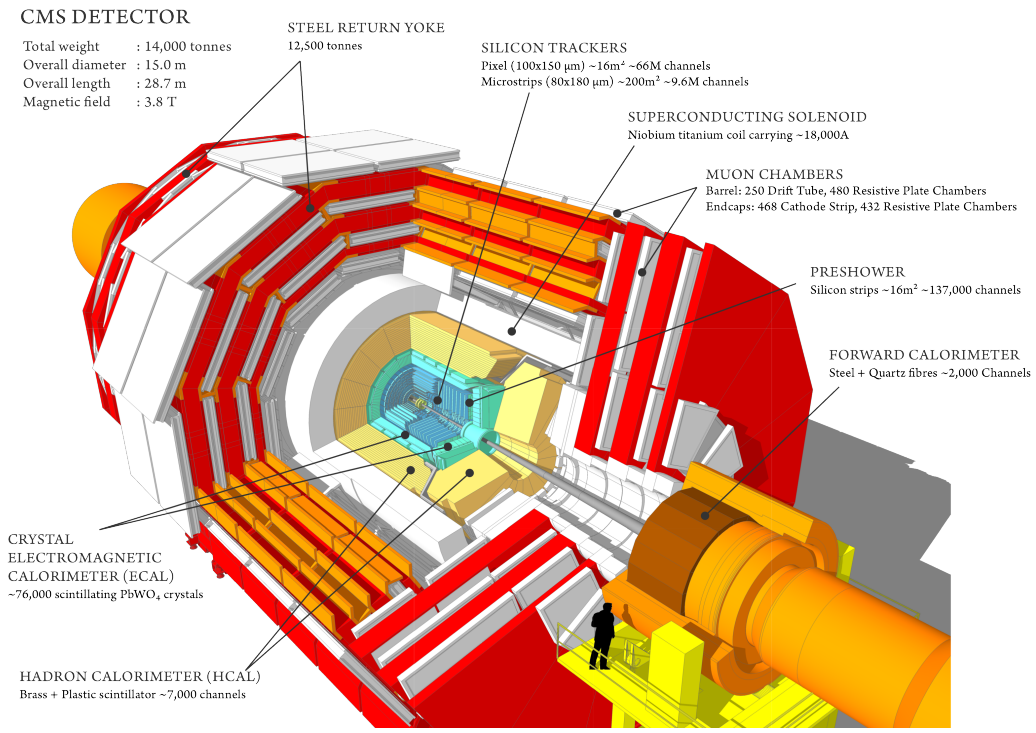

Figure 3.3: Layout of the CMS experiment and its sub-detectors.

3.2.1 Tracking detectors

The tracking system of CMS (Fig. 3.4) is designed to provide a precise and efficient measurement of the trajectories of charged particles emerging from the LHC collisions, as well as a precise reconstruction of secondary vertices [9]. It surrounds the interaction point and has a length of 5.8 m and a diameter of 2.5 m. In order to achieve high tracking efficiency at the high luminosities of LHC, a detector technology featuring granularity, speed and radiation hardness is required. Furthermore, the material budget of the tracking system has to be as low as possible in order to avoid a worsening of the tracking efficiency and resolution due to material interaction effects of the charged particle, such as multiple scattering, bremsstrahlung, photon conversion or nuclear interactions. These requirements lead to a tracker design entirely based on silicon detector technology. With about 200 m^2 of active silicon area the CMS tracker is the largest silicon tracker ever built. It is divided into a pixel detector close to the interaction region and a strip detector in the outer region. At LHC design luminosity more than 1000 particles are hitting the tracking volume in each bunch crossing. This leads to a hit rate density of 1 MHz/mm^2 at a radius of 4 cm which imposes severe challenges to the design of the tracking detectors. With a pixel size of 100×150 μm^2 in r-ϕ and z, respectively, an occupancy of the order of 10^{-4} per pixel and LHC bunch crossing can be achieved. The hit rate density falls with the distance from the interaction point to 60 kHz/mm^2 at a radius of 22 cm and to 3 kHz/mm^2 at a radius of 115 cm. Therefore, at intermediate radii (20–55 cm), silicon micro-strip detectors are used, with a typical cell length of 10 cm and a pitch of 80 μm. At the outermost radii (55-110 cm) the strip size can be further increased to 25 cm×180 μm. With this choice an occupancy of less than 3% is maintained in the strip detector. However, the strip capacitance scales with its length and therefore the electronics noise is a linear function of the strip length as well, becoming not negligible in the outermost region where the strip size is the largest. In order to maintain a good signal to noise ratio of well above 10, CMS uses thicker silicon sensors for the outer tracker region (500 μm thickness as opposed to the 320 μm in the inner tracker) with correspondingly higher signal. To mitigate the radiation damage effects and prolong the lifetime of the detector modules, the tracking detectors are designed to run at subzero temperatures. The cooling is established using a mono-phase liquid cooling system with C_6F_{14} as cooling fluid. The whole tracker system operated at +4°C during Run 1. After this phase, several improvements have been implemented and an operative temperature of -15°C is currently maintained for Run 2.

3.2.2 The Electromagnetic Calorimeter

3.2.3 The Hadronic Calorimeter

3.2.4 The Muon System

3.2.5 The Trigger System

3.3 The CMS detector simulation

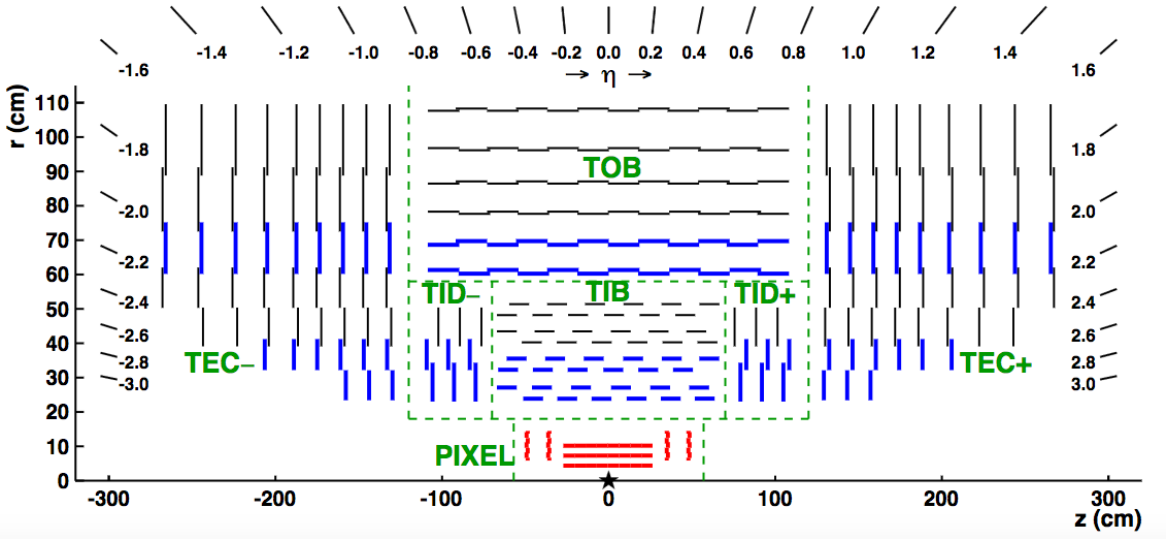

Figure 3.4: Longitudinal section of half of the CMS Tracker system; the different detector types are indicated.

Part I

Search for diboson resonances with CMS

Chapter 4

Diboson resonances as signature for new physics

Chapter 5

Event simulation

5.1 Monte Carlo event generators

5.2 Simulation of physics processes

5.2.1 Simulation of signal processes

5.2.2 Simulation of background processes

Chapter 6

Object and event reconstruction

6.1 Tracks and vertices

6.2 Electrons

6.3 Muons

6.4 Jets

6.4.1 Identification of b jets

6.5 Missing transverse energy

6.6 W$\rightarrow \ell\nu$ reconstruction

Chapter 7

Boosted H→$b\bar{b}$ and W/Z→$q\bar{q}^{(\prime)}$ identification with jet substructure

---

7.1 Jet substructure algorithms

7.1.1 Jet pruning

7.1.2 N-subjettiness

7.2 W/Z-tagging validation in top enriched sample

7.3 H-tagging algorithm

Chapter 8

Final event selection and categorization

8.1 Search for a WH resonance in the $\ell\nu b\bar{b}$ final state at $\sqrt{s}$ = 8 TeV

8.1.1 $t\bar{t}$ background rejection

8.1.2 Final selection and control plots

8.2 Search for WW/WZ resonances in the $\ell\nu q\bar{q}^{(\prime)}$ final state at $\sqrt{s}$ = 13 TeV

8.2.1 W/Z-jet mass categories

8.2.2 Final selection and control plots

Chapter 9

Background modeling

9.1 W+jets background estimate with alpha method

9.1.1 Description

9.1.2 Extraction of the W+jets normalization

9.1.3 Extraction of the W+jets shape

9.2 Top quark production

9.3 Systematic uncertainties in the background estimation

Chapter 10

Signal modeling and statistical treatment

10.1 Signal modeling

10.1.1 Parametrization of the resonance mass

10.1.2 Signal efficiency

10.2 Systematic uncertainties in the signal prediction

10.3 Testing new resonance hypothesis

10.3.1 Profile likelihood procedure

10.3.2 The CL_s method

10.3.3 Treatment of uncertainties

Chapter 11

Results with 8 TeV data

11.1 Final m_{WH} distribution

11.2 Studies on the excess

11.3 Significance of the data

11.4 Cross section limits

Chapter 12

Results with 13 TeV data

12.1 Final m_{WV} distribution

12.2 Cross section limits

Chapter 13

Combination of searches for diboson resonances at $\sqrt{s} = 8$ and 13 TeV

13.1 Inputs to the combination

13.1.1 8 TeV VV searches

13.1.2 13 TeV VV searches

13.1.3 8 TeV VH searches

13.1.4 13 TeV VH searches

13.2 Combination procedure

13.3 Results

13.3.1 Limits on W'

13.3.2 Limits on Z'

13.3.3 Limits on heavy vector triplet (W'+Z')

13.3.4 Limits on Bulk Graviton

13.3.5 Significance at 2 TeV

Chapter 14

Conclusions

Part II

Calibration and Upgrade of the CMS Pixel Barrel Detector

Chapter 15

introduction chapter: why pixels are so important for physics

Chapter 16

The CMS Pixel Barrel Detector

16.1 Design of the CMS Pixel Barrel Detector

16.2 Detector modules

16.2.1 Sensor

16.2.2 Readout Chip

16.2.3 Token Bit Manager

16.3 Readout and control system

16.3.1 Analog readout chain

16.3.2 Front End Driver

16.3.3 Supply Tube

16.3.4 Communication and Control Unit

16.3.5 Front End Controller

16.4 Pixel Online Software

16.5 Performance at $\sqrt{s} = 8$ and 13 TeV

Chapter 17

Optimization and commissioning for LHC Run II

17.1 Radiation damage after LHC Run I

17.2 Optimization for LHC Run II

17.2.1 Overview of pixel calibrations

17.2.2 Temperature dependence

17.3 Commissioning for LHC Run II

17.3.1 Installation into CMS

17.3.2 Check out of optical connections

17.3.3 Adjustment of readout chain settings

17.3.4 Optimisation of signal performance

Chapter 18

Phase I Upgrade of the CMS Pixel Barrel Detector

18.1 Motivations

18.2 Summary of changes

18.3 The digital readout chain

18.4 The Phase I supply tubes

18.5 The test stand

18.6 Supply tubes assembly and commissioning

18.7 Detector commissioning

Chapter 19

Conclusions

Part III

Summary

Bibliography

[1] L. Evans and P. Bryant, "LHC Machine", *JINST* **3** (2008) S08001.

[2] ATLAS Collaboration, "The ATLAS Experiment at the CERN Large Hadron Collider", *JINST* **3** (2008) S08003, doi:10.1088/1748-0221/3/08/S08003.

[3] CMS Collaboration, "The CMS experiment at the CERN LHC", *JINST* **3** (2008) S08004, doi:10.1088/1748-0221/3/08/S08004.

[4] LHCb Collaboration, "The LHCb Detector at the LHC", *JINST* **3** (2008) S08005, doi:10.1088/1748-0221/3/08/S08005.

[5] ALICE Collaboration, "The ALICE experiment at the CERN LHC", *JINST* **3** (2008) S08002, doi:10.1088/1748-0221/3/08/S08002.

[6] F. Marcastel, "CERN's Accelerator Complex. La chane des acclrateurs du CERN",. General Photo.

[7] CMS Collaboration, "CMS Public Luminosity Results". https://twiki.cern.ch/twiki/bin/view/CMSPublic/LumiPublicResults.

[8] N. Cartiglia, "Measurement of the proton-proton total, elastic, inelastic and diffractive cross sections at 2, 7, 8 and 57 TeV", arXiv:1305.6131.

[9] CMS Collaboration CollaborationV. Karimki, et al., "The CMS tracker system project: Technical Design Report". Technical Design Report CMS. CERN, Geneva, 1997.